



Characterization of gallium arsenide X-ray mesa *p-i-n* photodiodes at room temperature



G. Lioliou^{a,*}, X. Meng^b, J.S. Ng^b, A.M. Barnett^a

^a Semiconductor Materials and Devices Laboratory, Department Engineering and Design, Sch. of Engineering and Informatics, University of Sussex, Falmer, Brighton BN1 9QT, UK

^b Department of Electronic & Electrical Engineering, University of Sheffield, Mappin Street, Sheffield S1 3JD, UK

ARTICLE INFO

Article history:

Received 16 September 2015

Received in revised form

19 November 2015

Accepted 14 December 2015

Available online 22 December 2015

Keywords:

Gallium Arsenide

p-i-n photodiodes

X-ray spectroscopy

Visible and near infrared responsivity

ABSTRACT

Two GaAs mesa *p⁺-i-n⁺* photodiodes intended for photon counting X-ray spectroscopy, having an *i* layer thickness of 7 μm and diameter of 200 μm, have been characterized electrically, for their responsivity at the wavelength range 580 nm to 980 nm and one of them for its performance at detection of soft X-rays, at room temperature. Dark current and capacitance measurements as a function of applied forward and reverse bias are presented. The results show low leakage current densities, in the range of nA/cm² at the maximum internal electric field (22 kV/cm). The unintentional doping concentration of the *i* layer, calculated from capacitance measurements, was found to be < 10¹⁴ cm⁻³. Photocurrent measurements were performed under visible and near infrared light illumination for both diodes. The analysis of these measurements suggests the presence of a non-active (dead) layer (0.16 μm thickness) at the *p⁺* side top contact interface, where the photogenerated carriers do not contribute to the photocurrent, possibly due to recombination. One of the diodes, D1, was also characterized as detector for room temperature photon counting X-ray spectroscopy; the best energy resolution achieved (*FWHM*) at 5.9 keV was 745 eV. The noise analysis of the system, based on spectra obtained at different shaping times and applied reverse biases, showed that the dominant source of noise is the dielectric noise. It was also calculated that there was at least (165 ± 24) eV charge trapping noise at 0 V.

© 2016 The Authors. Published by Elsevier B.V. This is an open access article under the CC BY license (<http://creativecommons.org/licenses/by/4.0/>).

1. Introduction

GaAs detectors have a number of advantages over traditional and widely used narrow bandgap semiconductor materials, such as Si and Ge. The relatively wide bandgap of GaAs (1.42 eV) results in fewer thermally generated carriers compared to narrower bandgap materials and thus, lower leakage current densities, allowing X-ray detection at room temperature and above, with good energy resolution [1]. Consequently, the cooling system that is often required for Si and Ge detectors can be eliminated. This can decrease the cost, mass, volume and power consumption of spectrometers based on the devices. Space science applications, such as future missions to Mercury (extreme thermal environment [2]), Europa's oceans (hot hydrothermal vents [3]) and Jupiter (intense radiation environment [4]), and terrestrial applications outside the laboratory environment, have restrictions on mass, power and volume, and hence may benefit from the use of GaAs or other wide bandgap detectors. Moreover, the high mean atomic

number of GaAs provides higher detection efficiency for the same thickness compared with Si.

Researches have also proven a high radiation resistance of GaAs detectors to γ-rays [5,6], fast neutrons [7] and high energy electrons [8]. GaAs detectors are more radiation-resistance than Si for γ-rays, electrons and for low energy protons and neutrons [9]. As a result, GaAs is a suitable semiconductor material for radiation detection in environments which suffer from high radiation doses, such as space missions. However, it should be noted that GaAs is less radiation resistant than Si for high energy hadrons [9,10].

Results characterizing GaAs *p⁺-i-n⁺* mesa X-ray photodiodes grown by molecular beam epitaxy have been reported for soft X-ray spectroscopy (2 μm and 3 μm *i* layer thickness in [11,12] respectively) and for beta particle spectroscopy (2 μm *i* layer thickness in [13]). In this paper, results from two fully etched 200 μm diameter GaAs *p⁺-i-n⁺* mesa X-ray photodiodes with 7 μm thick *i* layers are presented. No thicker than 7 μm GaAs mesa *p⁺-i-n⁺* diodes have been reported in the literature to date. The wafer was grown by metal organic chemical vapour deposition at the EPSRC National Centre for III-V Technologies and the devices were fabricated at University of Sheffield. The devices reported in

* Corresponding author. Tel.: +44 1273 872568.

this paper were randomly selected from the wafer. In Section 2, the device structure is described. In Section 3, both devices are electrically characterized in terms of their current and capacitance at room temperature and key parameters are calculated. The devices are further characterized for their visible and near infrared responsivity without any external bias applied, and the results are presented in Section 4, along with theoretical calculations. The spectroscopic X-ray photon counting performance achieved with one GaAs $p^+ - i - n^+$ detector coupled with low-noise front-end electronics, operating at room temperature is reported and analysed in Section 5.

2. Device structure

GaAs epilayers were grown on a $350\ \mu\text{m}$ thick heavily doped, n^+ GaAs substrate by metal organic vapour deposition. The thickness of the unintentionally doped i layer was $7\ \mu\text{m}$, and it was grown between a $1\ \mu\text{m}$ n type and a $0.5\ \mu\text{m}$ p type GaAs layer. The p and n type dopants used were carbon and silicon, and the doping density of both n type and p type layers was $2 \times 10^{18}\ \text{cm}^{-3}$. The wafer's layer structure is summarised in Table 1 and a drawing of the structure can be seen in Fig. 1. Mesa diodes with diameters of $200\ \mu\text{m}$ were chemically etched using $\text{H}_3\text{PO}_4:\text{H}_2\text{O}_2:\text{H}_2\text{O}$ as the chemical etchant. The etched depth, as measured from the top of the wafer, was $8.3\ \mu\text{m}$. The Ohmic contact of the p side was formed from Ti ($20\ \text{nm}$ thickness) and Au ($200\ \text{nm}$ thickness) layers.

The quantum efficiency of the devices was calculated for photon energies up to $30\ \text{keV}$ and can be seen in Fig. 2. For these calculations it was assumed that there was a dead region at the p^+ layer, close to the surface with a width of $0.16\ \mu\text{m}$ (see Section 4). The rest of the p layer and the i layer was assumed to be the active region of the devices.

3. Electrical characterization

3.1. Current–voltage measurements

Both forward and reverse bias dark current measurements as functions of applied voltage (I – V characteristics) were measured using a Keithley 6487 Picoammeter/Voltage Source. The dark current at room temperature was measured for both diodes when forward biased in the range $0\ \text{V}$ to $1.5\ \text{V}$, and when reverse biased in the range $0\ \text{V}$ to $-15\ \text{V}$. Fig. 3 shows the forward I – V characteristics of diodes D1 and D2.

The ideality factor, n , and the saturation current, I_0 , were both calculated from the semi-logarithm I – V characteristics of the devices. These extracted values, as well as their temperature dependence reveal the nature of the conduction mechanism (thermionic emission, diffusion, recombination and tunnelling).

There are two distinct regions in Fig. 3. The first region which corresponds to applied voltages $V_a \leq 0.9\ \text{V}$, is the linear region. The saturation current, I_0 , was found to be $(3.12 \pm 0.32) \times 10^{-13}\ \text{A}$ and $(2.58 \pm 0.30) \times 10^{-13}\ \text{A}$ for diode D1 and diode D2 respectively. The ideality factor was computed to be 1.91 ± 0.01 for D1 and

Table 1
Layers structure of the GaAs $p^+ - i - n^+$ wafer.

Material	Type	Thickness (nm)	Doping density (cm^{-3})
GaAs	p^+	10	1×10^{19}
GaAs	p^+	500	2×10^{18}
GaAs	i	7000	Undoped
GaAs	n^+	1000	2×10^{18}
GaAs	n^+ (substrate)	–	–

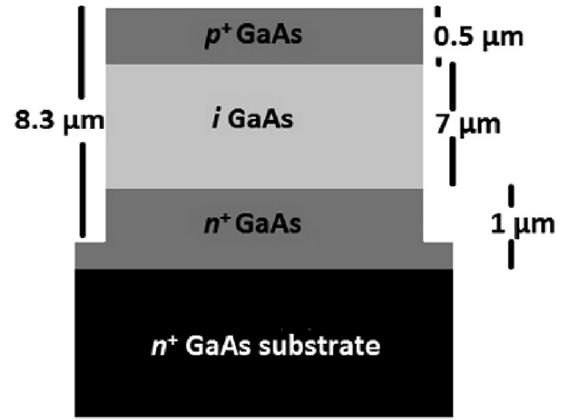


Fig. 1. Illustrative layers structure (not in scale) of the GaAs $p^+ - i - n^+$ diode.

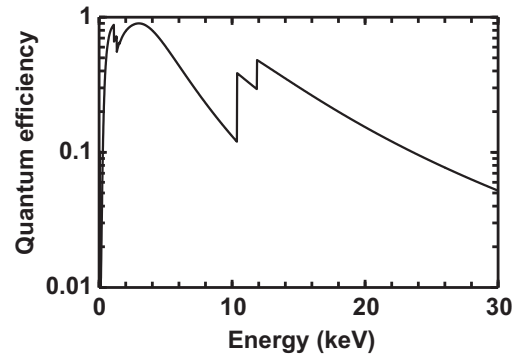


Fig. 2. Calculated quantum efficiency of the GaAs $p^+ - i - n^+$ mesa photodiodes as a function of photon energy.

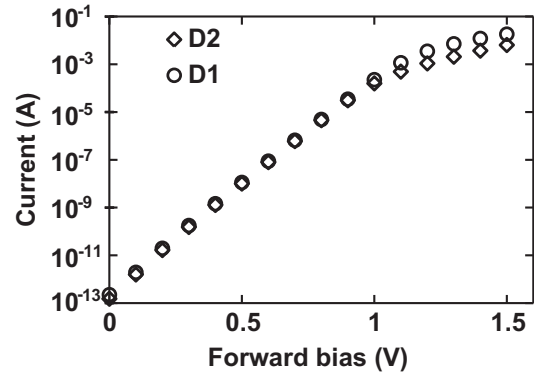


Fig. 3. Current as a function of applied forward bias of the two GaAs $p^+ - i - n^+$ mesa photodiodes, D1 and D2, measured at room temperature.

1.89 ± 0.01 for D2. Ideality factor values close to two suggest that the recombination current dominates [14]. Further investigation of the relationship between the ideality factors of each photodiode with temperature could give a better indication of the conduction process [15]. Such measurements and analysis will be reported separately in a future manuscript. The second region of the semi-logarithm I – V characteristics which corresponds to applied voltages $V_a > 0.9\ \text{V}$ deviates from linearity. As the applied voltage increased, the semi-logarithm I – V characteristics of the devices bend down (Fig. 3), resulting in a non-linear relationship between the logarithm of forward current and the applied voltage and indicating that the effect of series resistance, R_s , became significant.

The reverse I – V characteristics of the two GaAs $p^+ - i - n^+$ mesa photodiodes are shown in Fig. 4.

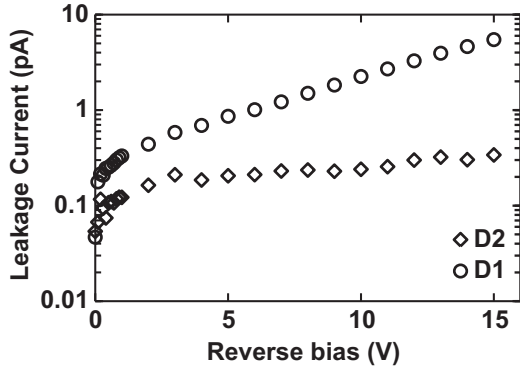


Fig. 4. Leakage current at room temperature as a function of applied reverse bias for the two GaAs p^+-i-n^+ mesa photodiodes, D1 and D2.

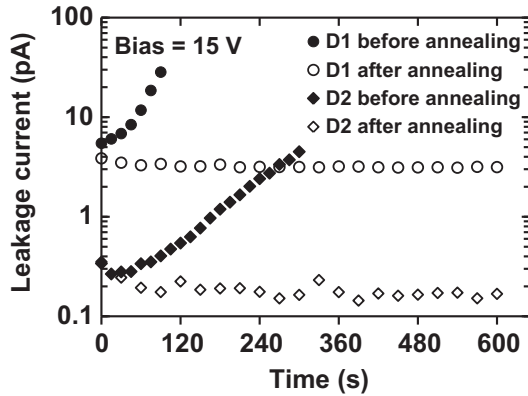


Fig. 5. Leakage current of two GaAs p^+-i-n^+ mesa photodiodes, D1 and D2, measured at 20 °C at 15 V reverse bias, as a function of time, before and after annealing at 120 °C.

Both GaAs p^+-i-n^+ mesa photodiodes showed low leakage current densities when biased at 15 V (mean electric field of 22 kV/cm across the i region). More specifically, at room temperature, the measured leakage current densities at 15 V reverse bias of D1, and D2 were 17.4 nA/cm² and 1.08 nA/cm², respectively. These values are broadly comparable with other high quality GaAs $p-i-n$ photodiodes (e.g. ~ 10 nA/cm² at 30 °C, at a similar internal electric field [1]), and are better than other reported similar GaAs p^+-i-n^+ mesa photodiodes having the same i layer thickness (20–100 nA/cm² at similar electric field and at room temperature [16]), possibly due to better wafer quality and diode fabrication.

The stability of the leakage current with time was investigated. Initial measurements at room temperature showed that the leakage current of diode D1 increased from 5.47 pA to 28.35 pA over a period of 90 s when reverse biased at 15 V. Under these conditions, the diode was not reverse biased at 15 V for more than 90 s to prevent damage to it. The leakage current of diode D2 was found to increase from 0.33 pA to 4.5 pA over a period of 300 s when reverse biased at 15 V. Both devices, D1 and D2, were then annealed up to a final temperature of 120 °C in a TAS Micro MT climatic cabinet. After annealing, they were gradually cooled to 20 °C, over a period of 205 min. The I - V measurements of the diodes were then repeated. The leakage current of D1 at 15 V reverse bias decreased from 5.47 pA to 3.86 pA, whereas no difference was observed in the leakage current of D2 at 15 V. Fig. 5 shows the measured leakage current of diodes D1 and D2 as a function of time, at 15 V reverse bias, both before and after annealing. After annealing, when reverse biased at 15 V the leakage current of both devices remained stable with time, over a period of 600 s. The precise mechanism of leakage current

reduction and leakage current stabilization over time, after heating the devices at 120 °C, is currently unknown, but the improvement can probably be attributed to the presence of shallow and/or deep level traps in GaAs being partially annealed by the heating. These traps (crystal defects), which might have been introduced during the growth or the processing of the devices, may be acting as generation-recombination centres and affecting the leakage current. Radiation induced defects have been previously shown to be annealed at -23 °C and at 227 °C [17], and at 40 °C [5] resulting in the recovery of the device properties. Similarly to this, crystal defects might have been partially annealed at 120 °C resulting in leakage current reduction.

3.2. Capacitance–voltage measurements

The depletion width and the doping concentrations in the intrinsic layer of the devices were determined from capacitance measurements. The capacitance was measured as a function of applied forward and reverse bias, using an HP 4275 A Multi Frequency LCR metre. The test signal was sinusoidal with a 50 mV rms magnitude and 1 MHz frequency. Capacitance measurements were made at reverse voltages between 0 V and -15 V and at forward voltages between 0 V and +1 V. The capacitance of the empty packaging was also measured and subtracted from the measured capacitance of the packaged diodes. The capacitance of the package was determined by measuring two empty packages and was found to be 0.6 pF. Fig. 6 shows the reverse and forward bias C - V characteristics of the two GaAs p^+-i-n^+ mesa photodiodes (packaging capacitances subtracted).

The depletion layer width of the diodes as a function of applied reverse voltage, $W(V)$, was computed using the measured depletion layer capacitance, $C(V)$, where

$$C(V) = \frac{\epsilon_0 \epsilon A}{W(V)} \quad (1)$$

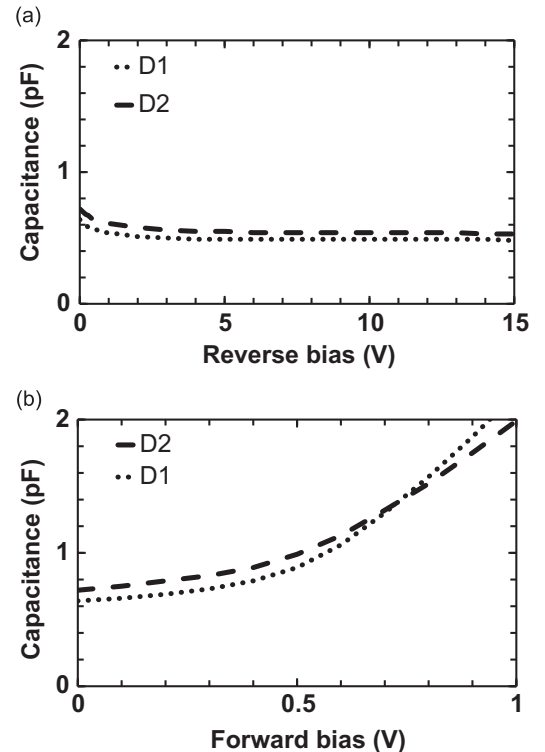


Fig. 6. Capacitance as a function of (a) reverse bias and (b) forward bias of the two GaAs p^+-i-n^+ mesa photodiodes, D1 and D2, measured at 20 °C.

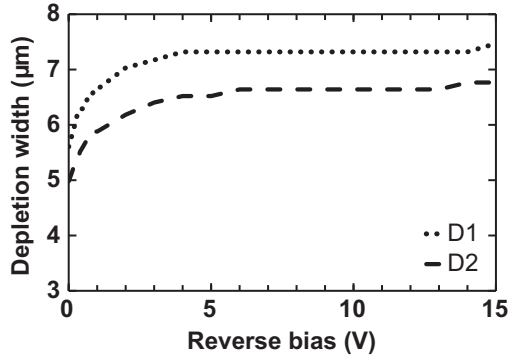


Fig. 7. Calculated depletion width for the two GaAs p^+i-n^+ mesa photodiodes calculated from capacitance measurements as a function of applied reverse bias.

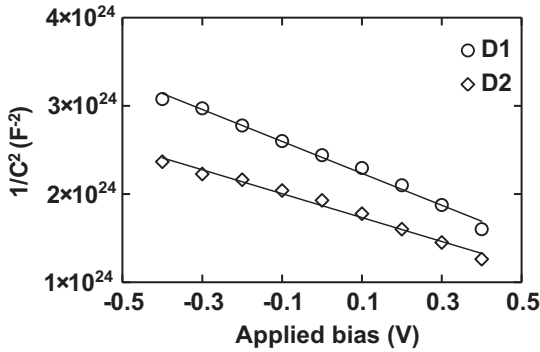


Fig. 8. C^{-2} as a function of applied voltage, V_a , for D1 (open circles) and D2 (open diamonds) at the bias range -0.5 V to 0.5 V where the relationship is linear. The line of best fit, for each set of data, calculated using linear least squares fitting, is also shown.

and ϵ_0 is the permittivity of free space, ϵ is the dielectric constant of GaAs and A is the area of the device [14]. The calculated depletion width of the two diodes is presented in Fig. 7. Once the lightly doped intrinsic layer is fully depleted, the capacitance is independent of the applied reverse bias. This occurred at -4 V reverse bias for D1, suggesting a depletion width of (7.3 ± 0.4) μm and at -6 V reverse bias for D2, suggesting a derived depletion width of (6.6 ± 0.4) μm . The depletion width at 0 V reverse bias was measured to be (5.6 ± 0.3) μm for D1 and (5.0 ± 0.2) μm for D2. The uncertainties of the calculated depletion widths were related to the uncertainty in the capacitance measurements (≤ 0.05 pF). Although Fig. 7 shows a small increase in the depleted depth from 14 V to 15 V reverse bias, this increase is insignificant because the spatial resolution of profiles determined by C - V measurements are of the order of a Debye length, which has been calculated for GaAs at room temperature to be 0.4 μm [14].

The built-in potential, V_{bi} , along with the doping level of the i layer, N_i , was calculated based on their relationship with the measured capacitance, given by ref. [18]. Fig. 8 shows the C^{-2} (V_a) relationship for the two fully etched GaAs p^+i-n^+ mesa photodiodes, D1 and D2, for the bias range -0.5 V to 0.5 V.

A line of best fit was calculated for the C^{-2} (V_a) data presented in Fig. 8 using linear least squares fitting. The value of V_{bi} was extracted from the voltage axis intercept point and the i layer doping density, N_i , from the gradient of the line. The measured built-in potential was (1.33 ± 0.05) V for D1 and (1.37 ± 0.06) V for D2. This is comparable with the theoretical built-in voltage based on the acceptor and donor density of the p^+ and n^+ layer respectively [14] ($=1.39$ V). Furthermore, the i layer doping density was calculated to be $(6.13 \pm 1.10) \times 10^{13}$ cm^{-3} for D1 and $(8.19 \pm 1.32) \times 10^{13}$ cm^{-3} for D2.

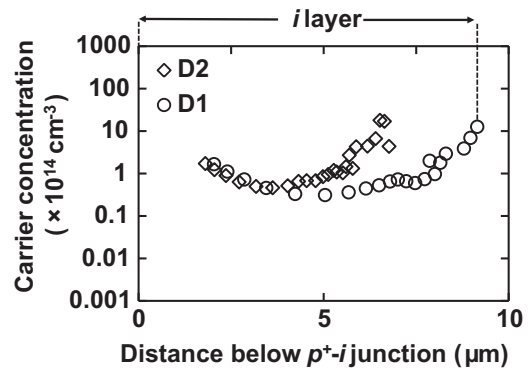


Fig. 9. Leakage current of two GaAs p^+i-n^+ mesa photodiodes, D1 and D2, measured at 20 $^\circ\text{C}$ at 15 V reverse bias, as a function of time, before and after annealing at 120 $^\circ\text{C}$.

Due to the high doping concentrations of the p^+ and n^+ layers, the extension of the depletion region to the p^+ and n^+ sides is negligible for the devices reported here. The doping profile (doping density as a function of distance below the p^+i junction) of the i layer, was also calculated (based on the capacitance measurements, using the equation for general nonuniform distributions) and is shown in Fig. 9 [14]. Because the data presented in Fig. 9 is based on C - V measurements and the maximum forward applied bias was 1 V, the lower limit in the distance below the p^+i junction at which the doping density can be calculated was 1.7 μm .

The lowest doping level in the i layer was found to be from 2.2 μm to 6.2 μm below the p^+i junction for D1 and from 2.2 μm to 5.0 μm below the p^+i junction for D2. At deeper distances (closer to $i-n^+$ junction), the doping level in the i layer increased reaching a maximum value of $\approx 1 \times 10^{15}$ cm^{-3} at the $i-n^+$ interface for both diodes, where the $i-n^+$ interface was determined from the capacitance measurements as a function of applied bias.

4. Visible and near infrared responsivity

4.1. Photocurrent measurements

To investigate the performance of the detectors under visible and near infrared light illumination, photocurrent measurements were made using a ThermoSpectronic UV300 UV-Vis spectrophotometer with Tungsten, Deuterium and Mercury lamps to cover the wavelength range 580 – 980 nm, in 5 nm intervals. The selection of the wavelength of interest was performed using an internal monochromator and UV grating. Custom baffles were used in order to ensure that no external sources of light could influence the measurements. The measured photocurrent, in the investigated wavelength range of 580 nm to 980 nm, was from < 1 pA to ≈ 35 pA.

Responsivity measurements of the two devices, in arbitrary units, are shown in Fig. 10 as a function of the incident photons' wavelengths, measured at room temperature and at 0 V reverse bias. The responsivity is a function of the wavelength (see theoretical analysis below). This is due to the dependence of the absorption coefficient of the material, α , on the incident light's wavelength [19].

The responsivity of the detectors exhibited abrupt spectral cutoff (GaAs direct bandgap= 1.42 eV [14]), as other semiconductors with direct bandgaps [20]. The long wavelength cutoff, which is established by bandgap, was 870 nm for both detectors [14], where the maximum responsivity was recorded. For wavelengths longer than 870 nm, the photon energy was smaller than

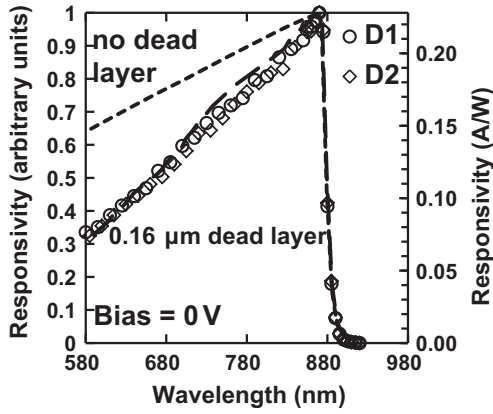


Fig. 10. Theoretical responsivity as a function of wavelength for dead layer thickness, $t_{dl}=0 \mu\text{m}$ (short dashes) and $t_{dl}=0.16 \mu\text{m}$ (long dashes), along with the measured responsivity of D1 (open circles) and D2 (open diamonds), all in arbitrary units. The theoretical responsivity for dead layer thickness, $t_{dl}=0.16 \mu\text{m}$ is also shown in A/W. Although the responsivity of D1 and D2 was measured with 5 nm intervals, a subset (15 nm intervals) of the experimental points is shown in this figure to improve clarity.

the bandgap energy so that no photoelectron was generated. The photoresponsivity decreased with shortening wavelength, from a maximum at 870 nm. This was attributed to the fact that the photons were absorbed near to the surface (penetration depth $< 1.2 \mu\text{m}$). The recombination lifetime is short near the surface [19], and hence some photocarriers recombined before being collected.

4.2. Theoretical responsivity

The theoretical responsivity as a function of wavelength, at the wavelength range of interest (580 nm to 980 nm) was calculated. The responsivity defined as the ratio of the photocurrent to the optical power, was computed based on the calculated quantum efficiency, n [14]. The quantum efficiency, defined as the number of electron hole pairs generated per photon incident on the diode [21], was calculated for each wavelength by

$$n = (1 - r) \left(\prod m \exp(-a_m t_m) \right) n_{\text{int}}. \quad (2)$$

The quantum efficiency as defined here should not be confused with the number of electron hole pairs generated per absorbed photon, which is related to the electron hole pair creation energy. The first term of (2), where r is the reflectance at each wavelength, describes the transmittance of the light at the air-photodiode interface [14]. The third term of (2), describes the absorption at the depletion region, being represented by the internal quantum efficiency, n_{int} . The internal quantum efficiency, giving the probability of a photon which has reached the top of the active layer (width W) being absorbed in this region [14], was computed using the equation

$$n_{\text{int}} = \left(1 - \frac{\exp(-a_{\text{GaAs}} W)}{1 + a L_p} \right), \quad (3)$$

where L_p is the hole diffusion length [14] ($= 1.2 \mu\text{m}$ in n type GaAs with a dopant concentration of $2 \times 10^{18} \text{cm}^{-3}$ [22]). Because the diffusion length of electrons is greater than the thickness of the p^+ layer [23], if there is no recombination region, the whole of the p^+ layer could be said to be active along with the i layer and the fraction of the n^+ layer determined by one hole diffusion length. Both the drift current (due to carriers generated inside the depletion region) and the diffusion current (due to carriers generated outside the depletion region and diffusing into the reverse biased junction) are taken into account in (3). The absorption coefficient, a , was related to the absorption index, k , and using the

values found in Ref. [24], it was computed as a function of wavelength.

The second term of (2) accounts for the absorption of photons before reaching the depletion region, at each m th layer. In the detectors' geometry, there are two absorbing layers in front of the active region of the device. These are: 1) the metallization layer (primarily 200 nm of Au) on top of the p^+ layer as the form of the p^+ contact and 2) the dead layer at the p layer, close to the surface of the detector. Starting with 1), the Au layer covered 45% of each diode's face. Consequently, the second term of (2), for $m=1$ becomes: $\left[(1 - f_{\text{geo}}) e^{(-a_1 t_1)} + f_{\text{geo}} \right]$, where f_{geo} is the geometrical fill factor of the devices which equals the area directly exposed to the incoming beam ($= 55\%$ for these devices) and a_1 and t_1 are the absorption coefficient of Au and the thickness of the Au layer, respectively [21]. In the wavelength of interest, the term $e^{(-a_1 t_1)}$ was computed to be in the range 10^{-6} – 10^{-8} , hence almost all photons falling on this are of the diode face are absorbed at the Au layer. Consequently, the second term of (2), for $m=1$, is simplified to f_{geo} .

Concerning layer 2), the total thickness of the p^+ layer was $0.5 \mu\text{m}$. While in the ideal case the whole p^+ layer can be considered to be active, depending on material growth, there can be a dead layer, where surface recombination takes place [19]. For t_{dl} being the thickness of the dead layer at the p side with an absorption coefficient a_{GaAs} , the second term of (2), for $m=2$ becomes $e^{(-a_{\text{GaAs}} t_{dl})}$.

The theoretical responsivity was computed as a function of wavelength, assuming there was no dead layer at the p^+ side, and can be seen in Fig. 10.

When no dead layer close to the surface of the detector was taken into account, agreement between the theoretical and the measured photoresponsivity was poor. Fig. 10 suggests that the difference between the measured responsivity at 580 nm (minimum) and 870 nm (maximum) is higher than the corresponding difference for the theoretical responsivity, meaning that the experimental responsivity at short wavelengths (penetration depth $< 1 \mu\text{m}$) was lower than the expected theoretical responsivity. One explanation for this would be the presence of a non-active (dead) layer at the p^+ side, where the photogenerated carriers do not contribute to the photocurrent, possibly due to recombination. Including the presence of a $0.16 \mu\text{m}$ thick dead layer in the model resulted in agreement between the theoretical and measured responsivity (Fig. 10). The maximum theoretical responsivity was found to be at 870 nm, reaching a value of 0.23 A/W for $t_{dl}=0.16 \mu\text{m}$, in contrast with 0.26 A/W for $t_{dl}=0 \mu\text{m}$, assuming any additional inefficiencies in detection in photons and charge transport losses are minimal.

5. X-ray spectroscopy and noise analysis

5.1. Measurements with an ^{55}Fe radioisotope X-ray source

To characterise the X-ray detection performance of the devices, X-ray spectra were obtained using device D1. An ^{55}Fe radioisotope X-ray source, with characteristic Mn $K\alpha$ (5.9 keV) and Mn $K\beta$ (6.49 keV) lines [25], was positioned 3 mm above the top of the diode. The diode was connected to a custom-made, single channel, charge sensitive preamplifier without the feedback resistor (similar to Ref. [26]). The diode and the preamplifier were kept at room temperature throughout the measurements. The signal of the preamplifier output was further shaped using an Ortec 572A shaping amplifier. The shaping amplifier was then connected to a multi-channel analyser (MCA). The live time limit for each accumulated spectrum was 120 s.

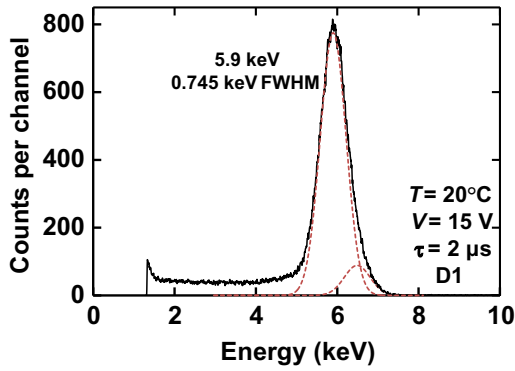


Fig. 11. ^{55}Fe spectrum accumulated with photodiode D1 at 15 V reverse bias ($\tau=2\ \mu\text{s}$) along with the fitted Mn $K\alpha$ and $K\beta$ peaks (dashed lines).

The diode was in turn reverse biased at 0 V, 5 V, 10 V and 15 V. At each reverse bias, X-ray spectra were obtained with varied shaping time, τ ($=0.5\ \mu\text{s}$, $1\ \mu\text{s}$, $2\ \mu\text{s}$, $3\ \mu\text{s}$, $6\ \mu\text{s}$ and $10\ \mu\text{s}$). Fig. 11 shows the obtained ^{55}Fe spectrum at $2\ \mu\text{s}$ shaping time and 15 V reverse bias. The dashed lines in Fig. 11 represent the fitted Gaussians to the peak in the ratio appropriate for ^{55}Fe [25] and taking account of the relative difference in efficiency of the detector for 5.9 keV and 6.49 keV X-rays. The detected ^{55}Fe photopeak is the combination of the Mn $K\alpha$ and Mn $K\beta$ lines, at 5.9 keV and 6.49 keV respectively [25], due to the energy resolution being insufficient to resolve the individual lines. The position of the zero energy noise peak and the position of the fitted Mn $K\alpha$ peak were used for energy calibration for each spectrum. In Fig. 11, the counts of the zero energy noise peak of the preamplifier were limited by setting the MCA low energy cut-off at 1.3 keV, however a small portion of the right hand side of the tail can still be seen in Fig. 11.

The low energy tailing of the combined Mn $K\alpha$ and Mn $K\beta$ peaks, which can be seen in Fig. 11, may be attributed to partial charge collection of charge created in the non-active layers, as per Ref. [27]. The amount of low energy tailing can be quantified by the valley-to-peak (V/P) ratio. The V/P ratio was measured for all obtained spectra from the ratio between counts at 3 keV and counts at 5.9 keV, a mean value of 0.05 was found; this value is comparable to that reported in Ref. [11]. The $FWHM$ at 5.9 keV was measured for all obtained spectra and is presented in Fig. 12(a)–(d) as a function of shaping time at 0 V, 5 V, 10 V and 15 V reverse bias, respectively.

The best energy resolution ($FWHM$) achieved was 745 eV at $2\ \mu\text{s}$ shaping time and 15 V reverse bias. The form of the plots in Fig. 12 indicates that the optimum shaping time for all reverse voltages was $1\ \mu\text{s}$ – $2\ \mu\text{s}$. At short shaping times, $\tau \leq 3\ \mu\text{s}$, as the reverse bias increased from 0 V to 15 V, better $FWHM$ at 5.9 keV was achieved. This was attributed to reduced charge trapping at high electric field strengths. However, at shaping times longer than $3\ \mu\text{s}$, the $FWHM$ of the photopeak at 15 V was equal (at $6\ \mu\text{s}$) or higher (at $10\ \mu\text{s}$) than the $FWHM$ of the photopeak at 0 V. The increase in leakage current, from 0.04 pA at 0 V to 3.86 pA at 15 V, resulted in larger parallel white noise, which outweighed the reduced charge trapping noise at long shaping times. The noise sources contributing to the energy resolution are discussed in the next section.

5.2. Noise analysis

The energy resolution of any semiconductor detector, measured by the $FWHM$ of the photopeak, is defined by three mechanisms (sources of noise), which all degrade its resolution [21]. The quadratic sum of these independent terms gives the energy

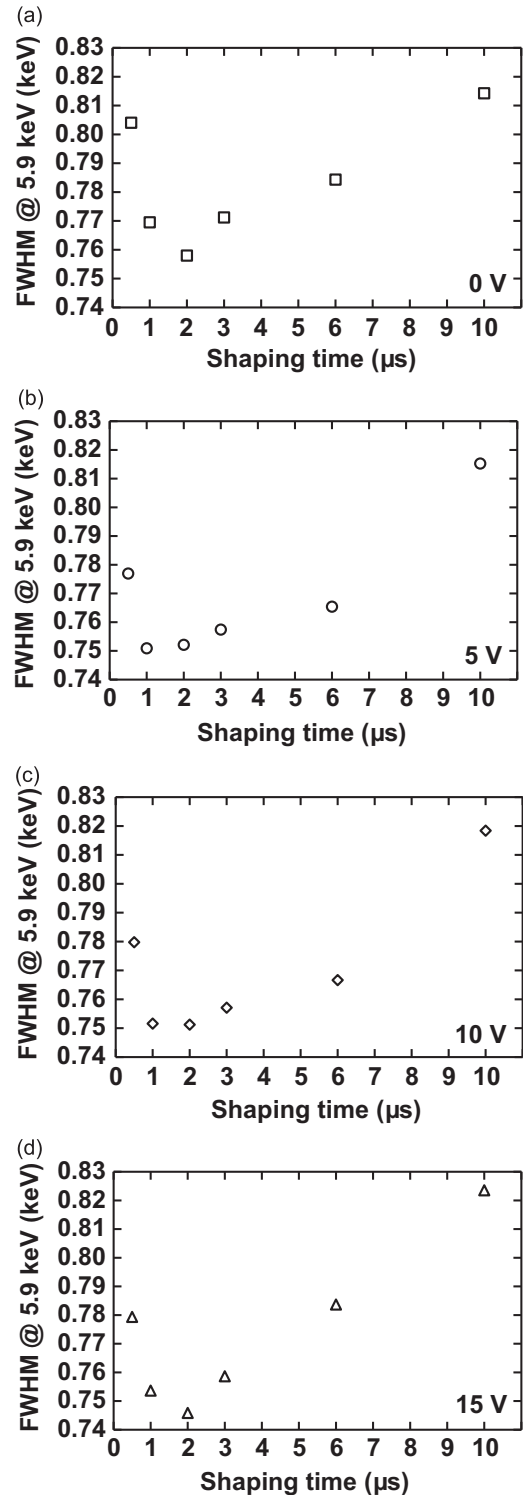


Fig. 12. Measured $FWHM$ at 5.9 keV for D1 as a function of shaping time at, (a) 0 V (squares); (b) 5 V (circles); (c) 10 V (diamonds); and (d) 15 V (triangles), reverse bias.

resolution, ΔE ,

$$\Delta E = 2.355\omega\sqrt{FE/\omega + R^2 + A^2}. \quad (4)$$

The first term under the square root, the Fano noise, is related to the statistical nature of the ionization process [28], the second term, R , represents the charge trapping noise arising from the incomplete charge collection, and the third term, A , represents the

broadening of the peak due to electronics noise. In (4), ω is the electron hole pair creation energy ($=4.184$ eV for GaAs [29]), F is the Fano Factor ($=0.12$ for GaAs [30]) and E is the photon energy [2]. Given that the Fano noise, expected to be 128 eV at 5.9 keV in GaAs (assuming $F=0.12$, and $\omega=4.184$ eV), is much smaller than the measured energy resolution, there are clearly significant noise contributions beyond the statistical generation of charge carriers as quantified by the Fano noise.

The electronics noise, due to the detector itself and the pre-amplifier, comprises parallel white noise, WP , series white noise (including the induced gate current noise), WS , $1/f$ noise, and dielectric noise, D . The first three noise components were calculated as described in Ref. [31], where more details about the noise sources can be found. The leakage current of the detector (Fig. 4) and the leakage current of the input JFET of the preamplifier (estimated to be ~ 10 pA under the specific bias conditions for the preamplifier [32]), give rise to the parallel white noise. The capacitance of the detector (including the capacitance of its packaging) and the capacitance of the input JFET of the preamplifier (estimated to be ~ 1.5 pF [32]) give rise to the series white noise. The noise sources that cannot be directly calculated are the dielectric noise, D , and the charge trapping noise, TR . However, by subtracting the calculated white series noise, white parallel noise, $1/f$ noise and the Fano noise in quadrature from the total $FWHM$ of the photopeak, the rest can be attributed to the quadratic sum of the dielectric noise and the charge trapping noise, $(D^2 + TR^2)^{1/2}$, both of which would normally be expected to be shaping time invariant for $0.5 \mu\text{s} \leq \tau \leq 10 \mu\text{s}$ and this detector. The total noise along with the calculated contributions of the above noise sources as a function of shaping time, at 15 V reverse bias, can be seen in Fig. 13.

The series white noise contribution decreases with increasing shaping time, whereas the opposite is true for parallel white noise, and the $1/f$ noise contribution is independent of shaping time [31]. Fig. 13 indicates that the quadratic sum of dielectric noise and charge trapping noise is the dominant noise contribution in the reported system. This combination was found to be independent of shaping time and with a mean value of (704 ± 3) eV (rms deviance). Since the dielectric and charge trapping noises cannot be individually detangled from the present measurements, it can only be said that one of them or both are the most significant noise sources at all shaping times at 15 V, and indeed at all reverse applied biases. This is in agreement with previous reports of systems using comparable detectors and preamplifier electronics [27,33]. The total measured noise and the computed quadratic sum of dielectric noise and charge trapping noise as a function of applied reverse bias, at an indicative shaping time of $10 \mu\text{s}$, is shown in Fig. 14.

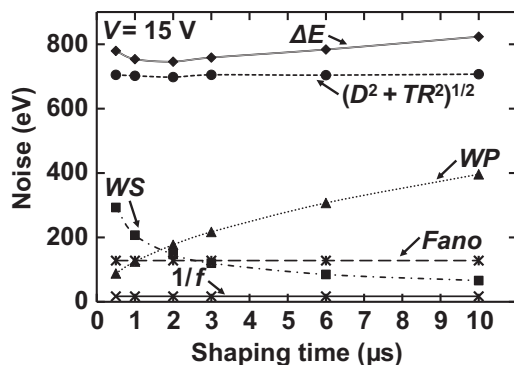


Fig. 13. Total $FWHM$ of the 5.9 keV peak (diamonds) with the quadratic sum of dielectric noise and charge trapping noise (circles), series white noise (squares), parallel white noise (triangles), Fano noise (stars) and $1/f$ noise (crosses) for D1 at 15 V reverse bias, as a function of shaping time. Lines are guides for the eyes only.

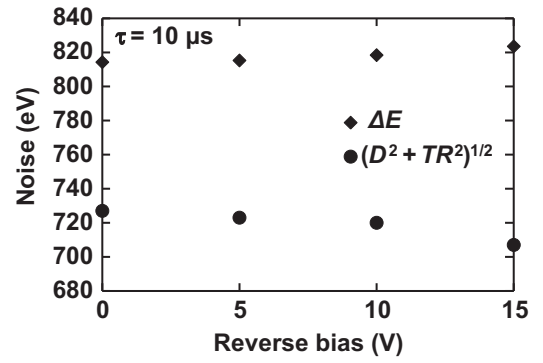


Fig. 14. Total $FWHM$ of the 5.9 keV peak (diamonds) with the calculated quadratic sum of dielectric and charge trapping noise (circles), for D1 at $10 \mu\text{s}$ shaping time as a function of applied reverse bias.

Although there was an increase in the total noise as the reverse bias was increased from 0 V to 15 V, the corresponding contribution of the dielectric and charge trapping noise decreased (see Fig. 14). The increase in the total noise was attributed to the larger parallel white noise at 15 V compared to 0 V. Although the dielectric noise does not vary with detector reverse bias, this is not the case for the charge trapping noise. Increased reverse bias (greater electric field strengths) can result in improved charge transport and less trapping noise. The same trend of the quadratic sum of the dielectric and charge trapping noise with reverse bias, as shown in Fig. 14 for $10 \mu\text{s}$ shaping time, was observed for all investigated shaping times. From these measurements, it was therefore possible to estimate the additional charge trapping noise present when the detector operates at 0 V compared to 15 V. A comparison between the contribution of both the dielectric noise and the charge trapping noise at 0 V and at 15 V, as a function of shaping time can be seen in Fig. 14.

The quadratic sum of dielectric and charge trapping noise was found to be (723 ± 5) eV at 0 V and (704 ± 3) eV at 15 V (see Fig. 15a). Thus, it was calculated that the additional charge trapping noise present when the detector was reverse biased at 0 V compared to 15 V was (165 ± 24) eV (with the increase in uncertainty being due to combining errors). Consequently, from Fig. 15a it can be said that the lower limit of charge trapping noise at 0 V reverse bias was (165 ± 24) eV (see Fig. 15b) and that the upper limit of the dielectric noise was (704 ± 3) eV at all reverse biases and at all shaping times.

The energy resolution (745 eV $FWHM$ at 5.9 keV at 15 V reverse bias) of the detector reported here is better than previously reported for other $7 \mu\text{m}$ GaAs devices (1 keV [16]), and slightly better than thinner ($2 \mu\text{m}$ and $3 \mu\text{m}$) GaAs $p^+ - i - n^+$ mesa photodiodes (≈ 800 eV [11,12]), coupled to similar front-end electronics as used for the currently reported devices. However, it is far from the best experimental reports of GaAs detectors at room temperature (300 eV [34] and 266 eV [35] $FWHM$ at 5.9 keV). The very good performance reported in Refs. [34,35] have yet to be replicated; they were probably due to exceptionally good epilayer quality and the low electronic noise of the system (242 eV [35]). Even though the electronics noise present in the system reported here is significant, making the $FWHM$ significantly greater than the Fano limited energy resolution, the preamplifier used is specialist for the specific application, low noise (~ 40 e $^-$ rms without detector), and has better performance than commercially available preamplifiers for detectors made from wide bandgap materials such as GaAs. Low noise electronics are even more critical than it is for Si and narrow bandgap materials due to the typically greater electron hole pair creation energies of wide bandgap materials. The dielectric noise, arising from the dielectrics around the input of the preamplifier, such as the package of the JFET [31], may be

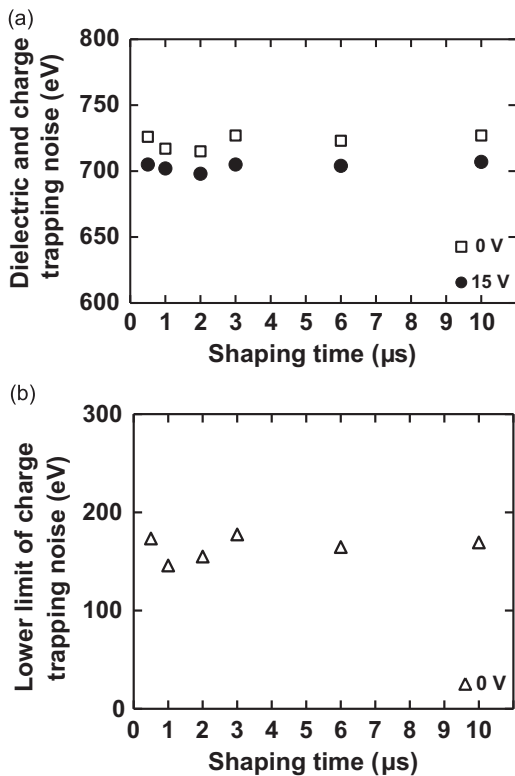


Fig. 15. (a) The calculated quadratic sum of dielectric and charge trapping noise at 0 V (open squares) and 15 V (filled circles) for D1 as a function of shaping time and b) the corresponding lower limit of charge trapping noise at 0 V.

the dominant source of noise limiting the energy resolution of the detector. It was estimated that if the dielectric noise could be eliminated, the energy resolution ($FWHM$ at 5.9 keV) would be reduced to 264 eV, which is similar to the energy resolution of the best reported system with a GaAs detector [35]. The dielectric noise computed for the current used preamplifier, having an upper limit of (704 ± 3) eV ($72 e^-$ rms), is comparable with previously reported results for similar front-end electronics (~ 700 eV in Ref. [33]).

6. Discussions, conclusions and future work

Two randomly selected 200 μm diameter GaAs mesa $p^+ - i - n^+$ photodiodes with 7 μm i layers have been electrically characterized at room temperature and their responsivity in the wavelength range 580 nm to 980 nm as well as the performance of one of them as detector for photon counting X-ray spectroscopy were investigated.

The dominant current mechanism of the devices was found to be recombination. Low leakage current densities were measured for both devices (17.4 nA/cm^2 for D1 and 1.08 nA/cm^2 for D2) at room temperature, at an internal electric field of 22 kV/cm. The leakage currents of the devices as functions of time were found to stabilise after annealing the detectors at 120 °C. The i layer thickness and doping concentration of the devices were deduced from capacitance measurements. It was found that D1 had a (7.3 ± 0.4) μm thick i layer with a doping density of $(6.13 \pm 1.10) \times 10^{13} \text{ cm}^{-3}$ and D2 had a (6.6 ± 0.4) μm thick i layer with a doping density of $(8.19 \pm 1.32) \times 10^{13} \text{ cm}^{-3}$.

Visible and near infrared responsivity measurements suggested the presence of a dead layer at the face of the devices with a thickness of 0.16 μm , in which the generated carriers from photon absorption do not contribute to the photocurrent. The maximum

theoretical responsivity of the devices was calculated to be 0.23 A/W at 870 nm.

Results from X-ray spectroscopy at room temperature with an ^{55}Fe source using one of the diodes were reported as functions of applied reverse bias and shaping time. The best energy resolution ($FWHM$ at 5.9 keV = 745 eV) was achieved at 2 μs , at 15 V reverse bias. Subsequent noise analysis showed that there was at least (165 ± 24) eV charge trapping noise at 0 V and that the dominant source of noise was the dielectric noise, with an upper limit of (704 ± 3) eV. Although this energy resolution is modest compared to the best reported results for GaAs detectors (300 eV by Erd et al. [34] and 266 eV by Owens et al. [35]), importantly, it was predicted that the energy resolution of the detectors would become similar to those reported in Refs. [34,35], if the noise of the dielectrics could be eliminated. In future publications, characterization of the temperature dependence of the performance of the detectors will be reported as will work to improve the resolution of the system by reducing the dielectric noise contribution through novel redesign of the preamplifier frontend and packaging.

Acknowledgements

This work was supported in part by STFC grants ST/M002772/1 and ST/M004635/1, Royal Society grant RS130515 (University of Sussex, A.M. Barnett PI) and by EPSRC grant EP/I010920/1 (University of Sheffield, J.S. Ng PI). The work of J.S. Ng was supported by a Royal Society University Research Fellowship. The work of G. Lioliou was supported by a Ph.D. scholarship from University of Sussex.

References

- [1] G. Bertuccio, R. Casiraghi, D. Maiocchi, A. Owens, M. Bavdaz, A. Peacock, H. Andersson, S. Nenonen, IEEE Transactions on Nuclear Science NS50 (2003) 723.
- [2] A. Owens, A. Peacock, Nuclear Instruments and Methods in Physics Research Section A 531 (2004) 18.
- [3] R.P. Lowell, M. DuBose, Geophysical Research Letters 32 (2005) L05202.
- [4] J.L. Barth, C.S. Dyer, E.G. Stassinopoulos, IEEE Transactions on Nuclear Science NS50 (2003) 466.
- [5] V.K. Dixit, S.K. Khamari, S. Manwani, S. Porwal, K. Alexander, T.K. Sharma, S. Kher, S.M. Oak, Nuclear Instruments and Methods in Physics Research Section A 785 (2015) 93.
- [6] T. Ly Anh, A. Perd'ochová, V. Nečas, V. Pavlicová, Nuclear Physics B - Proceedings Supplements 150 (2006) 402.
- [7] M. Ladziánský, A. Šagátová, V. Nečas, F. Dubecký, V. Linhart, Nuclear Instruments and Methods in Physics Research Section A 607 (2009) 135.
- [8] A. Šagátová, B. Zát'ko, M. Pavlovič, K. Sedláčková, P. Hybler, F. Dubecký, V. Nečas, Journal of Instrumentation 9 (2014) C04036.
- [9] L. Rossi, P. Fischer, T. Rohe, N. Wermes, Pixel Detectors: From Fundamentals to Applications, Springer, Heidelberg, Berlin, 2006.
- [10] P.J. Sellin, J. Vaitkus, Nuclear Instruments and Methods in Physics Research Section A 557 (2006) 479.
- [11] A.M. Barnett, J.E. Lees, D.J. Bassford, J.S. Ng, C.H. Tan, N. Babazadeh, R.B. Gomes, Nuclear Instruments and Methods in Physics Research Section A 654 (2011) 336.
- [12] A.M. Barnett, Nuclear Instruments and Methods in Physics Research Section A 756 (2014) 39.
- [13] A.M. Barnett, J.E. Lees, D.J. Bassford, Journal of Instrumentation 7 (2012) P09012.
- [14] S.M. Sze, Physics of Semiconductor Devices, 3rd ed., John Wiley & Sons, New Jersey, 2007.
- [15] A. Sellai, In: Proceedings of the IEEE International Conference on Semiconductor Electronics, Johor, Malaysia, 25 November–27 November 2008, pp. 267–270.
- [16] J.S. Ng, X. Meng, J.E. Lees, A. Barnett, C.H. Tan, Journal of Instrumentation 9 (2014) T08005.
- [17] H.J. Stein, Journal of Applied Physics 40 (1969) 5300.
- [18] X. Chen, H. Zhu, J. Cai, Z. Wu, Journal of Applied Physics 102 (2007) 024505.
- [19] B.E.A. Saleh, M.C. Teich, Fundamentals of Photonics, John Wiley & Sons Inc, New York, 1991.

- [20] J.T. Torvik, J.I. Pankove, B.J. Van Zegbroeck, IEEE Transactions on Electron Devices NS46 (1999) 1326.
- [21] G.W. Fraser, X-ray Detectors in Astronomy, Cambridge University Press, Cambridge, 1989.
- [22] C.J. Hwang, Journal of Applied Physics 40 (1969) 3731.
- [23] D.R. Wight, P.E. Oliver, T. Prentice, V.W. Steward, Journal of Crystal Growth 55 (1981) 183.
- [24] E.D. Palik, Handbook of Optical Constants of Solids, Academic Press, Burlington, 1997.
- [25] U. Schötzg, Applied Radiation and Isotopes 53 (2000) 469.
- [26] G. Bertuccio, P. Rehak, D. Xi, Nuclear Instruments and Methods in Physics Research Section B 326 (1993) 71.
- [27] A.M. Barnett, G. Lioliou, J.S. Ng, Nuclear Instruments and Methods in Physics Research Section A 774 (2015) 29.
- [28] G. Bertuccio, IEEE Solid-State Circuits Magazine 4 (2012) 36.
- [29] G. Bertuccio, D. Maiocchi, Journal of Applied Physics 92 (2002) 1248.
- [30] G. Bertuccio, A. Pullia, J. Lauter, A. Forster, H. Luth, IEEE Transactions on Nuclear Science NS44 (1997) 1.
- [31] G. Bertuccio, A. Pullia, G. De Geronimo, Nuclear Instruments and Methods in Physics Research Section A 380 (1996) 301.
- [32] Anon, N-Channel JFETs: 2N4416. Vishay Intertechnology, Inc. United States, 2005.
- [33] A.M. Barnett, J.E. Lees, D.J. Bassford, J.S. Ng, Nuclear Instruments and Methods in Physics Research Section A 673 (2012) 10.
- [34] C. Erd, A. Owens, G. Brammertz, M. Bavdaz, A. Peacock, V. Lämsä, S. Nenonen, H. Andersson, N. Haack, Nuclear Instruments and Methods in Physics Research Section A 487 (2002) 78.
- [35] A. Owens, M. Bavdaz, A. Peacock, A. Poelaert, H. Andersson, S. Nenonen, H. Sipila, L. Tröger, G. Bertuccio, Journal of Applied Physics 90 (2001) 5376.